

University of Wollongong

Research Online

Australian Institute for Innovative Materials -
Papers

Australian Institute for Innovative Materials

1-1-2020

A High-Kinetics Sulfur Cathode with a Highly Efficient Mechanism for Superior Room-Temperature Na-S Batteries

Zichao Yan

University of Wollongong, zy820@uowmail.edu.au

Yaru Liang

Jin Xiao

Weihong Lai

University of Wollongong, weihongl@uow.edu.au

Wanlin Wang

University of Wollongong, ww268@uowmail.edu.au

See next page for additional authors

Follow this and additional works at: <https://ro.uow.edu.au/aiimpapers>



Part of the [Engineering Commons](#), and the [Physical Sciences and Mathematics Commons](#)

Research Online is the open access institutional repository for the University of Wollongong. For further information contact the UOW Library: research-pubs@uow.edu.au

A High-Kinetics Sulfur Cathode with a Highly Efficient Mechanism for Superior Room-Temperature Na-S Batteries

Abstract

2020 WILEY-VCH Verlag GmbH & Co. KGaA, Weinheim Applications of room-temperature-sodium sulfur (RT-Na/S) batteries are currently impeded by the insulating nature of sulfur, the slow redox kinetics of sulfur with sodium, and the dissolution and migration of sodium polysulfides. Herein, a novel micrometer-sized hierarchical S cathode supported by FeS₂ electrocatalyst, which is grown in situ in well-confined carbon nanocage assemblies, is presented. The hierarchical carbon matrix can provide multiple physical entrapment to polysulfides, and the FeS₂ nanograins exhibit a low Na-ion diffusion barrier, strong binding energy, and high affinity for sodium polysulfides. Their combination makes it an ideal sulfur host to immobilize the polysulfides and achieve reversible conversion of polysulfides toward Na₂S. Importantly, the hierarchical S cathode is suitable for large-scale production via the inexpensive and green spray-drying method. The porous hierarchical S cathode offers a high sulfur content of 65.5 wt%, and can deliver high reversible capacity (524 mAh g⁻¹ over 300 cycles at 0.1 A g⁻¹) and outstanding rate capability (395 mAh g⁻¹ at 1 A g⁻¹ for 850 cycles), holding great promise for both scientific research and real application.

Disciplines

Engineering | Physical Sciences and Mathematics

Publication Details

Yan, Z., Liang, Y., Xiao, J., Lai, W., Wang, W., Xia, Q., Wang, Y., Gu, Q., Lu, H., Chou, S., Liu, Y., Liu, H. & Dou, S. (2020). A High-Kinetics Sulfur Cathode with a Highly Efficient Mechanism for Superior Room-Temperature Na-S Batteries. *Advanced Materials*,

Authors

Zichao Yan, Yaru Liang, Jin Xiao, Weihong Lai, Wanlin Wang, Qingbing Xia, Yunxiao Wang, Qinfen Gu, Huanming Lu, Shulei Chou, Yong Liu, Hua-Kun Liu, and Shi Xue Dou

High-kinetics sulfur cathode with highly efficient mechanism for superior room-temperature Na-S batteries

Zichao Yan,¹ Yaru Liang,^{2,5} Jin Xiao,³ Weihong Lai,¹ Wanlin Wang,¹ Qingbing Xia,¹ Yunxiao Wang,^{*,1} Qinfen Gu,⁴ Huanming Lu,^{*,5} Shu-Lei Chou,^{*,1} Yong Liu,^{*,6} Huakun Liu,¹ and Shi-Xue Dou¹

¹Institute for Superconducting & Electronic Materials, Australian Institute of Innovative Materials, University of Wollongong, Innovation Campus, Squires Way, North Wollongong, New South Wales 2500, Australia. *Corresponding author email: yunxiao@uow.edu.au; shulei@uow.edu.au

²Central South University Powder Metallurgy Research Institute State Key Laboratory of Powder Metallurgy, Lushan South Road, Changsha, 410083, China

³School of Science, Hunan University of Technology, Zhuzhou 412007, China

⁴Australian Synchrotron, 800 Blackburn Road, Clayton, Victoria 3168, Australia

⁵Ningbo Institute of Materials Technology & Engineering, Chinese Academy of Sciences, Ningbo 315201, China. Email: hmlu@nimte.ac.cn

⁶School of Ophthalmology and Optometry, School of Biomedical Engineering, Wenzhou Medical University, Wenzhou 325027, China. Email: yongliu@wmu.edu.cn

Keywords: large-scale production, hierarchical structure, sodium-sulfur batteries, ferrous disulfide, nanograins

Abstract:

Applications of room-temperature sodium sulfur (RT-Na/S) batteries are currently impeded by the insulating nature of sulfur, the slow redox kinetics of sulfur with sodium, and the dissolution and migration of the sodium polysulfides. Herein, the authors present a novel micron-sized hierarchical S cathode supported by FeS₂ electrocatalyst that is grown *in situ* in well-confined carbon nanocage assemblies. The hierarchical carbon matrix can provide multiple physical entrapment to polysulfides, and the FeS₂ nanograins exhibit a low Na-ion diffusion barrier, strong binding energy, and high affinity for sodium polysulfides. Their combination makes it an ideal sulfur host to immobilize the polysulfides and achieve reversible conversion of polysulfides towards Na₂S. Importantly, the hierarchical S cathode is suitable for large-scale production via the inexpensive and green spray-drying method. The porous hierarchical S cathode offers a high sulfur content of 65.5 wt%, which can deliver high reversible capacity (524 mAh g⁻¹ over 300 cycles at 0.1 A g⁻¹) and outstanding rate capability

(395 mAh g⁻¹ at 1 A g⁻¹ for 850 cycles), holding great promise for both scientific research and real application.

Room-temperature sodium-sulfur (RT-Na/S) batteries are considered one of the most promising next-generation batteries and have aroused great research interest due to the low cost, abundance, nontoxicity, and high theoretical energy density (1274 Wh kg⁻¹) of sulfur.^[1] Their actual energy densities are a far cry from the theoretical values, however. Their practical applications are mainly impeded by the problematic S cathode due to its insulating nature and the slow redox kinetics of sulfur, as well as the dissolution and migration of the reaction intermediates (sodium polysulfide, Na₂S_x, 4 ≤ x ≤ 8).^[2] These drawbacks not only cause serious loss of active materials but also incomplete conversion reactions during charge/discharge processes, resulting in rapid capacity decay and poor reversible capacity.^[3] Many approaches have been introduced from their lithium-sulfur (Li/S) counterparts. The most popular strategy is to encapsulate sulfur in nanostructured carbon matrices, including carbon nanotubes,^[4] hollow carbon nanospheres,^[5] carbon nanofibers,^[6] and nanoporous carbon.^[7] Nevertheless, due to the nonpolar nature of the carbon hosts, they can only partially retain polysulfides by weak physical Van der Waals interaction. Very recently, it was found that polarized carbon hosts, produced via incorporating sulfiphilic sites, are much better than plain carbon matrices for enhancing S cathodes, owing to their strong chemical bonding to polysulfides.^[2] On one hand, fundamental researches on sulfiphilic species, such as TiO₂ and BaTiO₃,^[8] metallic Cu and Co,^[9] polyacrylonitrile,^[10] and Se-S composite,^[11] have been introduced in nanosized carbon to improve the electrochemical performance of RT-Na/S batteries, although progress is still impeded by the so-called shuttle-effects of sodium polysulfides. On the other hand, nanosized structure of the carbon host is certainly not a panacea from the applications perspective. Firstly, the troublesome synthesis approaches and the dimensions of nanoparticles with low yield are difficult for mass production. Secondly,

their high electrolyte/electrode surface area may lead to more difficulty in maintaining interparticle contact. Most importantly, the tap density of a nanopowder is generally less than for micron-size materials, resulting in the reduced volumetric energy density.^[12] Micron-size carbon hosts have not been utilized in RT-Na/S batteries for confining polysulfides, however, due to their inherent defects, including lower electrical conductivity, poor electrolyte infiltration, and limited pore volume when compared to nanosized hosts.^{[13] [14]} Therefore, it would be very challenging but highly profitable to realize a highly efficient S cathode that was suitable for facile and large-scale production toward practical RT-Na/S batteries.

In this work, we present a novel sulfiphilic host consisting of FeS₂ nanograins grown *in situ* in nitrogen-doped hierarchical carbon microspheres (FeS₂@NCMS) with high pore volume. After encapsulating S in the FeS₂@NCMS host, FeS₂@NCMS/S composite with a high S loading ratio can be achieved, which is expected to exhibit enhanced polysulfide immobilization and conversion as cathode in RT-Na/S batteries. First, such porous carbon microspheres offer high surface area (569 m² g⁻¹) and pore volume (0.98 cm³ g⁻¹) to support abundant N-doped electroactive sites and high theoretical loading mass of sulfur (70 wt %); and the interconnected carbon skeleton would facilitate the accessibility of those sulfiphilic sites to polysulfide. Second, the hierarchical microspheres are assembled from numerous nanocages that serve as containers for S species, which can effectively confine the dissolution and diffusion of polysulfides due to their excellent immobilizing effects derived from the well-confined space and buffered diffusion paths. Third, the FeS₂ electrocatalyst plays critical roles in optimizing the S cathode, because it shows strong chemical bonding and a fast redox mechanism for polysulfides, leading to high utilization of polysulfide reactions; moreover, the partially intercalated FeS₂ (Na_xFeS₂) during the initial discharge process could strengthen these effects of FeS₂ due to the enhanced electrical conductivity and adsorption energy. And the micron-size FeS₂@NCMS/S with uniform distribution can achieve high volumetric energy density compared to those of nanosized hosts. With favorable micro-/nano-

architectures and strong electrocatalysis, the synthesized high-kinetics FeS₂@NCMS/S cathode has been designed to exhibit high reversible capacity and lifespan, thus making a great leap forward for practical RT-Na/S batteries.

The synthetic strategy for the FeS₂@NCMS/S composite by a large-scale template-free approach is schematically illustrated in **Figure 1**. The precursor solution was prepared by well mixing the Fe source, β -cyclodextrin (β -CD), polyvinylpyrrolidone (PVP), and the N source additives, which can be used to produce spherical precursors by spray-drying. For a laboratory-scale spray dryer, the maximum capacity can be up to 2500 mL h⁻¹, which is suitable for quick and large-scale production (Figure S1 in the Supporting Information). β -CD is one of the well-known supramolecular compounds that are toroidal in shape with a hydrophobic inner cavity and a hydrophilic exterior.^[15] These unique characteristics can enable them to bind selectively various organic and inorganic molecules in their cavities and on their exterior to form stable inclusion complexes and nanostructured hollow assemblies. In this synthesis, benefiting from the high molecular selectivity and enantioselectivity of β -CD, the exterior hydroxyls of the β -CD molecule can form hydrogen bonds with PVP in water solution. Subsequently, the PVP coordinates to Fe³⁺ to form Fe-PVP- β -CD complexes with the inner cavity retained.^[16] The Fe-PVP- β -CD complex as a molecular template with a cavity structure is responsible for both structural control and pore formation, which finally form the hierarchical structure with hollow nanocage assemblies in microspheres during the carbonization process.

The X-ray diffraction (XRD) analysis in Figure S2 shows that the crystalline structures of Fe₃O₄ (35.5 and 43.1°), metallic iron (44.8°), and carbon (25.9°) were detected in the hierarchical precursor (Fe₃O₄-Fe@NCMS), indicating that the Fe source can be reduced to metallic iron during the carbonization process with partial oxidation. In the following sulfur loading process, the XRD pattern of the FeS₂@NCMS/S composite (average size of FeS₂: 6.7 \pm 0.8 nm) is dominated by the elemental sulfur with a high sulfur content of 65.5 wt%

(Figure S3a,b). It is interesting to note that the diffraction peaks of both iron oxide and metallic iron are disappeared, which means they were transferred to other materials during the high temperature sulfur loading process. Once the sulfur has been removed by immersing FeS₂@NCMS/S in CS₂ and further evaporating it in a furnace, the characteristic peaks of FeS₂ can be clearly observed, confirming that both the previously formed iron oxide and metallic iron can be sulfurized to FeS₂ during the sulfur loading process.^[17] The nitrogen absorption analysis of Fe₃O₄-Fe@NCMS revealed a high specific surface area of 569 m² g⁻¹, and a hierarchical porous structure with total pore volume of 0.98 cm³ g⁻¹ can be observed (Figure S3c). After the sulfur infusion, the values of the specific surface area and pore volume decrease to 130 m² g⁻¹ and 0.21 cm³ g⁻¹, respectively, which can be attributed to the distribution of S in both the hollow spaces and the pores of the host. The pore volume variation of 0.77 cm³ g⁻¹ was calculated to a maximum of 1.96 g of S embedded in the mesopores for each gram of the host, which is consistent with the thermogravimetric analysis (TGA) (Figure S3b). The sulfurization process during high temperature sulfur loading is also evidenced by X-ray photoelectron spectroscopy (XPS). There are six de-convoluted peaks for the Fe 2p XPS spectrum in Fe₃O₄-Fe@NCMS (Figure S4a). The four peaks respectively correspond to Fe²⁺ (710.9 and 724.8 eV) and Fe³⁺ (713.3 and 727.1 eV) in the Fe₃O₄ phase,^[18] while the other two peaks (706.6 and 719.3 eV) correspond to Fe⁰ of metallic iron.^[19] For the FeS₂@NCMS/S composite (Figure S4b), there are only two peaks located at 707.5 and 720.4 eV that can be assigned to the Fe 2p_{3/2} and Fe 2p_{1/2} binding energies in FeS₂, respectively.^[20] The two peaks in the S 2p spectrum (Figure S4c) at 162.4 and 163.8 eV are assigned to the 2p_{3/2} and 2p_{1/2} orbitals of S in FeS₂, while the peaks at 163.2 and 164.5 eV are ascribed to the spin-orbit coupling of elemental S.^[21] The above results indicate that the two iron species in Fe₃O₄-Fe@NCMS can be converted to FeS₂ during the sulfur loading process. The doped nitrogen (Figure S4d) leads to the dominance of pyridinic and pyrrolic nitrogen at 397.7-400.3 eV. The N-doped carbon could serve as a conductive Lewis base matrix, which is expected to

increase the adsorbability with respect to the polysulfides and promote the conversion kinetics.^[22]

The field-emission scanning electron microscopy (FESEM) image shows that the sulfur loaded product has a microsphere morphology with an average diameter of $\sim 1.1 \pm 0.1 \mu\text{m}$ (**Figure 2a**), which can provide a higher electron density, leading to a favorable volumetric energy density. The magnified FESEM and transmission electron microscope (TEM) images (Figure 2b,c) show that numerous nanocages derived from the Fe-PVP- β -CD complex are distributed in the microspheres and interconnected throughout the carbon skeleton. This interconnected hierarchical structure can not only improve the utilization of S, but also facilitates electron transfer inside the hierarchical microsphere. The TEM and scanning TEM (STEM) images indicate that there is a homogeneous distribution of FeS₂ nanoparticles coupled with nanocages that are embedded in the microspheric skeleton (Figure 2d, e). The TEM image of FeS₂@NCMS/S shows less transparency when compared with its Fe₃O₄-Fe@NCMS precursor (Figure S5), indicating the successful loading of sulfur. More electron microscopy techniques have been introduced in Figure S6 to characterize the hierarchical structure from the surface to the interior. It is interesting to note that the iron species, PVP, and β -CD play different roles in the formation of the hierarchical structure. The iron species are responsible for the robust spherical morphology at high temperature (Figure S7a), while PVP controls the size distribution of the nanoparticles (Figure S7b), and β -CD plays the key role in the formation of the pore structure (Figure S7c). The high-resolution TEM (HRTEM) image reveals that the lattice spacing of 0.336 nm, corresponding to graphitic carbon layers, is found near FeS₂ nanoparticles, which results from the catalytic graphitization of amorphous carbon by the formation of metallic iron during the carbonization process (Figure 2f).^[23] The existence of partially graphitized carbon is also evidenced by the Raman spectrum (Figure S8). The peaks located at 1340 and 1580 cm⁻¹ in the Raman spectrum are the characteristic D and G band peaks of carbonaceous materials. The Fe₃O₄-Fe@NCMS shows a two-dimensional

(2D) band peak and sharp D and G band peaks when compared with amorphous carbonized pure dextrin (CPD), indicating the presence of graphite with defects and disordered structure.^[24] The high-angle annular dark-field scanning transmission electron microscopy (HAADF-STEM) image of FeS₂@NCMS/S clearly reveals the distinct crystal and atomic arrangements of FeS₂ nanoparticles (Figure 2g). The interplanar spacing between adjacent lattice planes was measured to be 0.224 and 0.382 nm, corresponding to the (2-11) and (110) planes of FeS₂, respectively. The typical molecular models (inset) of FeS₂ along the [-113] projected direction coupled with the fast Fourier transform (FFT) pattern are also highly consistent with the pyrite phase, indicating a high degree of crystallinity for the FeS₂ nanograins (Figure 2h). The STEM energy dispersive spectroscopy (EDS) mapping images and line scanning (Figure 2i) of individual particles show the homogeneous distribution of Fe, N, and S elements along the C skeleton. The atomic concentrations of N and Fe in the composite are 1.92 and 9.36 %, respectively (Figure S9a). To further confirm that the sulfur has been encapsulated inside the host rather than absorbed on the surface, STEM-EDS mapping images of a cross-section of the FeS₂@NCMS/S cathode were obtained by the focused ion beam (FIB) technique. It is obvious that the elements (C, N, S, and Fe) are homogeneously distributed along the cross-section as well, indicating the homogeneous distribution of sulfur in both the surface and the interior due to the facilitated sulfur infiltration channels through the meso- and micropores (Figure S9b). The mass content of FeS₂ nanograins in the FeS₂@NCMS host was conducted by TGA under flowing air, which indicates that the overall content of FeS₂ nanoparticles in the hierarchical microspheres is 14.5 wt% (Figure S10). It is expected that the FeS₂@NCMS/S cathode with a hierarchical microspheric carbon skeleton and electrocatalytic effect based on the N-doped sites and FeS₂ nanograins could provide synergetic effects towards physical confinement and chemical bonding to immobilize the polysulfides in RT-Na/S batteries.

The assembled coin cells with FeS₂@NCMS/S cathode, a conventional current collector, and carbonate-based electrolyte were tested in the voltage window of 0.8-2.8 V. The Cyclic voltammograms (CVs) were recorded at a scan rate of 0.1 mV s⁻¹, as is shown in **Figure 3a**. There are two prominent peaks centred at 2.15 and 0.83 V during the first cathodic scan. The peak around 2.15 V can be attributed to the transition from elemental sulfur to long-chain polysulfides, and the soluble long-chain polysulfides are gradually transformed to less soluble short-chain Na₂S₄ in the following reactions.^[5] The sharp peak at 0.83 V corresponds to the formation of Na₂S and the solid-electrolyte interphase (SEI) layer during the further sodiation. In the following five cathodic scans, two major repeatable reduction peaks appear at 1.48 and 1.02 V, which correspond to the conversion of the dissolved Na₂S_x (4 < x ≤ 8) to Na₂S₄ and the formation of short-chain Na₂S₂ and Na₂S, and are highly repeatable without current attenuation, indicating a reversible reaction mechanism with high capacity retention in this system. It is interesting to note that the electrocatalyst-free cathode, the sulfur-loaded nitrogen-doped hierarchical carbon microsphere (NCMS/S), cathode shows obvious current attenuation and a less defined cathodic peak (around 1.5 V), caused by the loss of active material and the sluggish reactivity of sulfur towards sodium when compared to that of FeS₂@NCMS/S (Figure S11). This indicates that the FeS₂@NCMS/S electrode promises better electrochemical performance in RT-Na/S batteries with the assistance of strong adsorption capability of the FeS₂ nanograins. The charge/discharge plateau shown in Figure 3b can be clearly distinguished from the 1st to the 300th cycle at 0.1 A g⁻¹ for FeS₂@NCMS/S electrode. The discharge plateaus above 2.0 V and below 1.5 V for the initial cycle are attributed to the reduction from sulfur to long-chain polysulfides and the formation of short-chain polysulfides, respectively. Interestingly, the plateau above 2.0 V disappeared after the second cycle, whilst the well-defined plateau around 1.5 V became clear and was highly repeatable in the following cycles. This suggests that the transition between sulfur and the polysulfides is irreversible. Thus, the long-chain polysulfides Na₂S_x and the short-chain

polysulfides dominate the redox reactions in this RT-Na/S system. Based on this highly reversible mechanism, the FeS₂@NCMS/S electrode delivered a high initial capacity of 1471 mAh g⁻¹ and maintained a stable capacity of 524 mAh g⁻¹ over 300 cycles at a current density of 0.1 A g⁻¹ (Figure 3c). Remarkably, the FeS₂@NCMS/S composite delivered a reversible capacity of 395 mAh g⁻¹ for 850 cycles even at 1 A g⁻¹ (Figure S12). In the case of the electrocatalyst-free host (Figure S13), however, the NCMS/S electrode with a sulfur loading of 61.7 % showed a dramatic capacity loss of 60% based on the 2nd cycle after 300 cycles and a low retained capacity of 270 mAh g⁻¹ at 0.1 A g⁻¹ because of the polysulfide dissolution. The excellent cycling performance of the FeS₂@NCMS/S electrode, especially compared to the electrocatalyst-free cathode, is highly attributable to not only the strong chemical bonds between Na₂S_x and the polar surface, but also the fast reduction of long-chain polysulfides due to the FeS₂ electrocatalyst. The FeS₂@NCMS/S electrode also presented excellent rate performance, delivering reversible capacity of 624, 573, 533, 444, 340, and 139 mAh g⁻¹ at current densities of 0.1, 0.2, 0.5, 1, 2, and 5 A g⁻¹, respectively (Figure 3d). Upon reverting back to 0.1 A g⁻¹, the FeS₂@NCMS/S electrode shows a fully restored capacity of 581 mAh g⁻¹. Obviously, the FeS₂@NCMS/S presented much better high-rate capability as compared to the electrocatalyst-free cathode. To the best of our knowledge, this rate performance of the micron-size cathode, benefitting from the hierarchical physical entrapment and electrocatalytic anchoring of polysulfides, is competitive with the previously reported nano-size cathodes with a conventional current collector and carbonate-based electrolyte (Figure 3e). It is notable that a large irreversible capacity loss is observed in the initial cycle for both samples, and there is a gradual decay over the initial 50 cycles for the NCMS/S electrode. As discussed in Figure 3a and b, the large irreversible capacity between the initial and second cycles could be attributed to three major parts: (i) the irreversible transition between sulfur and the polysulfides; (ii) the loss of active material due to the dissolution of the surface polysulfides into the carbonate electrolyte; (iii) the formation of the solid-electrolyte

interphase (SEI) layer during the sodiation process in the low voltage.^[22] The limited capability for polysulfide immobilization of the S-host, however, is responsible for the capacity decay over the initial 50 cycles. As in the comprehensive comparison with previous reports that is presented in Figure 3e, FeS₂@NCMS/S shows outstanding results in terms of both its rate capability and its capacity retention relative to the 2nd cycle after the first 50 cycles. The successful polysulfide immobilization of the FeS₂@NCMS/S cathode can be assigned to not only the electrocatalytic effects of the encapsulated FeS₂ nanograins but also the well-designed hierarchical structures. The hierarchical spheres assembled from nanocages as interconnected containers for S species can effectively confine the dissolution and diffusion of polysulfides, due to their excellent immobilizing effects derived from the well-confined space and tortuous diffusion paths. To exclude capacity contribution of the S host, the FeS₂@NCMS electrode was tested, which showed a negligible capacity in the same conditions (Figure S14a). For comparison, a control sample without the hierarchical structure was prepared by conducting the same experiment without PVP and with the iron species removed by acid (Figure S14b). The carbon microspheres sulfur composite (CMS/S) without the hierarchical structure showed a low sulfur loading of 51.3 % (Figure S14c). It is electrochemically inactive with negligible reversible capacity, which is likely due to open pore structure of the CMS host (Figure S15a). The Nyquist spectrum of CMS/S after 30 cycles shows much higher charge transfer resistance (R_{ct}) than FeS₂@NCMS/S and NCMS/S (Figure S15b). When the cells were disassembled, the separator of CMS/S had become heavily yellow. The corresponding SEM images collected before and after cycling and cross-sectional EDS mapping images of CMS/S electrode showing thick film and pronounced crack formation in the cycled electrodes with concentrated signal of sodium on the surface (Figure S15c). Uniform dispersions of S and Na were observed, however, in both FeS₂@NCMS/S and NCMS/S. The open pore structure of CMS/S is proven to be responsible for its electrochemically inactive when compared to the well-confined NCMS/S, which caused the

formation of thick insulating layer and pronounced cracks in the carbonate electrolyte due to the heavy dissolution of polysulfides and volume expansion in the course of cycling. This phenomenon finally impeded Na^+ diffusion and electron transfer, which ultimately resulted in increased cell resistance. Furthermore, optically transparent RT-Na/S cells are shown in operation in Figure S16. After 8 h of discharging, a faint yellow color is observed in the transparent cell for the NCMS/S, which is due to the resultant polysulfide migration. In contrast, no obvious color change is observed for the $\text{FeS}_2\text{@NCMS/S}$. Based on the quite good results obtained from the transparent cell, we designed minitype pouch cells (0.1 Ah) with $\text{FeS}_2\text{@NCMS/S}$ cathodes and sodium coated copper foil anodes (Figure S17). After assembly, the pouch cells were discharged and charged repeatedly at a current density of 0.75 mA cm^{-2} . Overall, the cycling of $\text{Na|FeS}_2\text{@NCMS/S}$ pouch cells was stable, and the voltage profiles were identical to those of the coin cells, demonstrating the practicability of RT-Na/S batteries with the high-kinetics $\text{FeS}_2\text{@NCMS/S}$ cathode. These results further confirmed that the well-confined hierarchical structure and electrocatalyst greatly immobilized the dissolution and diffusion of polysulfides, guaranteeing the high kinetics and high performance of $\text{FeS}_2\text{@NCMS/S}$ cathode, as well as its practicability for the RT-Na/S system.

To gain insight into the mechanism and high kinetics of $\text{FeS}_2\text{@NCMS/S}$ in the highly reversible reactions, in-situ synchrotron XRD ($\lambda = 0.688111 \text{ \AA}$) carried out on the Powder Diffraction Beamline (Australian Synchrotron) was performed to investigate the charge/discharge products and intermediate phases of the RT-Na/ $\text{FeS}_2\text{@NCMS/S}$ cell (**Figure 4a**). There are three obvious peaks in the fresh cell. One of them, located at 6.91° , can be indexed to the (113) planes of elemental sulfur (JCPDS No. 77-0145). The other two at 14.97° and 16.25° are attributed to the (200) and (210) planes of FeS_2 (JCPDS No. 42-1340). The transition from S_8 to long-chain polysulfides (Na_2S_x) started at 2.1 V with extended shoulder at $6.7\text{-}6.8^\circ$ which is related to the generation of polysulfide species and detected through the organized adsorption of Na_2S_x at the ferrous disulfide surface of the hierarchical host.^[25]

During further discharging, a new peak at 13.8° appeared at 1.45 V, indicating the reaction from Na_2S_x to Na_2S_4 (JCPDS No. 71-0516). The thus-formed Na_2S_4 could be further reduced to Na_2S_2 (JCPDS No. 81-1771) with the discharge voltage from 1.45 to 1.2 V. The peaks of Na_2S_4 and Na_2S_2 gradually faded with the signal of Na_2S (JCPDS No. 77-2149) emerged, since further discharged to 1.1 V, which signify the final discharging product in this RT- $\text{Na}/\text{FeS}_2@\text{NCMS}/\text{S}$ cell. Therefore, combined with the CV analysis, the following picture is revealed: S_8 undergoes three intermediate phases (Na_2S_x , Na_2S_4 , and Na_2S_2) to reach the final product (Na_2S) in the initial discharge. When desodiated back to 2.0 V, the peaks of Na_2S_2 and Na_2S_4 are detected, demonstrating that the reverse conversions in this system. The signal of S_8 cannot be detected, however, even on full desodiation back to 2.8 V, suggesting the irreversibility of sulfur reduction. The working mechanism for RT- Na/S batteries are different from the high- and intermediate-temperature $\text{Na}-\text{S}$ batteries which the formation of solid Na_2S_2 dramatically increases the electrode resistance and prohibits any further discharge reaction.^[22] Firstly, in room-temperature $\text{Na}-\text{S}$ battery, the solid Na_2S_2 can be fully reduced to solid Na_2S benefit from the highly conductive framework provided by the host material. Besides, in room-temperature $\text{Na}-\text{S}$ battery, the plateau around 1.5 V is mainly corresponding to the conversion of the Na_2S_x ($4 < x \leq 8$) to Na_2S_4 , and the formation of Na_2S_2 and Na_2S can be assigned to the plateau around 1.0 V. It is worth to note that the diffraction peak intensity of Na_2S_2 become weak and disappeared in the following charge and discharge processes. This indicates that the oxidation rate of Na_2S_2 as it is transformed into Na_2S_4 and the reduction rate of Na_2S_2 into Na_2S are dramatically accelerated. Based on the above results, showing the benefit from the electrocatalytic effect of FeS_2 nanograins, we propose a two-step electrocatalytic mechanism, in which the redox reactions of polysulfides occur on the $\text{FeS}_2@\text{NCMS}/\text{S}$ electrode through two distinctive steps with Na_2S_2 as an intermediate. The polysulfides adsorbed on the polar surface of FeS_2 nanoparticles by tight chemical bonds first

undergo a sodiation process through the low diffusion barriers at the surface to form a Na_2S_2 intermediate, which is subsequently catalyzed to the final product, Na_2S . This reasonably analysis of the electrocatalytic effect shows that it could restrain the dissolution of Na_2S_4 by catalyzing it to insoluble short-chain polysulfides, and it promises better electrochemical performance of the $\text{FeS}_2@\text{NCMS}/\text{S}$ cathode in RT- Na/S batteries as well. The electrocatalytic behavior was further verified and highlighted via density functional theory (DFT) calculations to investigate the binding energies to polysulfides and diffusion barriers for Na ions on FeS_2 nanograins and the nitrogen-doped substrate. The optimized structure of the FeS_2 (0 0 1) surface for polysulfide adsorption behavior is shown in Figure 4b. The chemical interactions are dominated by the bonds between Na_2S_x and FeS_2 . As shown in Figure 4c, the binding energies of Na_2S_6 on FeS_2 and nitrogen-doped substrate are 1.32 and 0.55 eV (as listed in Table S1), respectively, which are much higher than that on the pure carbon dominated by van der Waals interactions (0.07 eV). More importantly, the binding energy of Na_2S_2 intermediate on FeS_2 is the highest at 2.78 eV, which is more than triple that on the nitrogen-doped substrate, indicating the possibility that Na_2S_2 intermediate has the fastest catalytic reaction in the RT- $\text{Na}/\text{FeS}_2@\text{NCMS}/\text{S}$ battery. Furthermore, we simulated the diffusion barriers for Na ions on the FeS_2 (0 0 1) surface with three different paths. Path 1 is along the *b*-axis (A \rightarrow B), as shown in Figure 4d. Path 2 is along the *a*-axis (B \rightarrow C), and path 3 is C \rightarrow A. The energy profiles along the individual paths for FeS_2 are shown in Figure 4e. It can be found that path 1 has the smallest diffusion barrier, which is only 0.071 eV. The diffusion barriers for paths 2 and 3 are 0.149 and 0.147 eV, respectively. On the FeS_2 (0 0 1) surface, S-Fe bonds form channels along the *b*-axis. So, Na ions are easier to transport via path 1 than paths 2 and 3. The former is along these channels, while the latter needs to climb the barrier of channels. It should be noted, however, that the barrier for the channels is very small (0.08 eV). So, the FeS_2 shows small Na ion diffusion barriers for all paths that lie the region of 0.071 to 0.149 eV (as listed in Table S2), presenting enhanced high kinetics for polysulfide redox reactions

based on the fast ion diffusion on the polar surface. Therefore, the diffusions in these three pathways have double-peak and single-peak profiles. This two-step electrocatalytic mechanism can benefit from both the strong binding energy of polysulfides and the low diffusion barrier on FeS₂ nanograins, as illustrated in Figure 4f. Firstly, the polar surface of FeS₂ as a catalytic site can strongly adsorb soluble long-chain polysulfides, which greatly promotes their nucleation. Secondly, as the fast-catalytic reaction goes on, the long-chain polysulfides quickly convert to short-chain polysulfides with boosted bonding energy. Once the Na₂S₂ intermediate has formed, the bonding energy increases to the highest 2.78 eV, and thus, the Na₂S₂ immediately decomposes to the final product Na₂S with a further boosted catalytic reaction.^[26] In comparison, the host without electrocatalysis (Figure 4g) suffers from a dramatic diffusion of long-chain polysulfides and incomplete conversion reactions due to the sluggish reaction kinetics of sulfur and its Na₂S product. This phenomenon is repeated in every subsequent cycle, which leads to the formation of a thick insulating layer, thus resulting in severe capacity fading, as illustrated in Figure S15.

To further visually demonstrate the anchoring ability of the hierarchical carbon microspheres and the above hypothesis, the sodiation/desodiation process of the hierarchical host was recorded using in-situ TEM (**Figure 5a**). Here, the nanocage assemblies as independent containers for S species effectively prevent the polysulfides from expanding out of the hierarchical sphere in sodiation/desodiation processes (Videos S1 and S2). The representative pristine FeS₂@NCMS/S shows a diameter of 535 nm. During the sodiation process (Figure 5b), the volume of the representative particle increased gradually as the sodiation time was extended, resulting in a slight volume expansion of 3.4 %. The volume almost fully recovers to the pristine state after full desodiation (Figure 5c). The slight volume variation and barely diffused polysulfide confirm that the interconnection of the nanocages and incorporation of FeS₂ electrocatalyst can prevent the expansion of sulfur species. In comparison, without the support of the hierarchical structure and polar component, the

polysulfides visibly spilled out of the CMS/S particles (Video S3). Notably, numerous nanocages in the hierarchical structure show variable transparency during the sodiation/desodiation process, indicating the quasi-solid state transitions of sulfur- Na_2S_x and Na_2S_x - Na_2S , respectively. After the initial sodiation process, the anchored Na_2S particles are visibly observed, indicating the highly efficient immobilization of the hierarchical structure. As shown in in-situ selected area electron diffraction (SAED) patterns (Figure 5d), the diffraction patterns of FeS_2 are observed in the pristine particle. And a new diffraction pattern with a recognizable reflection of the (220) planes of Na_2S is observed when Na ions are introduced into $\text{FeS}_2@\text{NCMS}/\text{S}$ for 255 s. With the sodiation process went on, more identified diffraction rings of Na_2S are clearly observed, which is in good agreement with the results of *in-situ* synchrotron XRD. Similar to lithium-sulfur batteries, the signal of those intermediate states can not be found by the *in-situ* TEM observation.^[23] Based on the previous work and our results, there are two potential causes for the phenomenon. On one hand, the poor thermal stability of sulfur and long-chain sodium polysulfides could be burned or melted by the zoomed electron beam, and the high thermal stability of Na_2S selectively retained. On the other hand, based on the reduction equation: $\text{Na}_2\text{S}_x + (2x-2)\text{Na}^+ + (2x-2)\text{e}^- = x\text{Na}_2\text{S}$, the zoomed electron beam could accelerate the reduction of long-chain sodium polysulfides to Na_2S with sufficient Na^+ and electron during the discharging process. The trace of Na_xFeS_2 is found to coexist with FeS_2 at 401 s in the sodiation process, demonstrating that the Na^+ partially intercalate into FeS_2 , based on the mechanism: $\text{FeS}_2 + x\text{Na}^+ + x\text{e}^- \rightarrow \text{Na}_x\text{FeS}_2$ (shown in detail by ex-situ STEM in Figure S18). The intercalation-type FeS_2 therefore has fast kinetics, since Na_xFeS_2 has high polaron mobility.^[27] Consequently, the affinity for polysulfides of the novel host can not only be attributed to the FeS_2 electrocatalyst and the conductive Lewis base matrix but also the hierarchical structure assembled from nanocages as well, thereby suppressing the shuttling effect and resulting in stable cyclability. This was also confirmed by ex-situ STEM-EDS mapping images (Figure S19) of the $\text{FeS}_2@\text{NCMS}/\text{S}$

electrode in the sodiated state, where the dispersion of sulfur greatly overlaps with sodium inside the host, illustrating the effective anchoring of sulfur species with high activity.

A hierarchical high-kinetics S cathode suitable for large-scale production has been synthesized in this paper. In-situ synchrotron XRD, in-situ TEM, and DFT results confirm that the hierarchical nano-/microstructure coupled with the effective FeS₂ electrocatalyst simultaneously achieved high reversible capacity and long lifespan for the FeS₂@NCMS/S cathode. Significantly, the soluble polysulfides can be strongly adsorbed and catalyzed on the polar surfaces of FeS₂ nanograins. They undergo a fast sodiation process to form Na₂S₂ intermediate through the polar surface with low diffusion barriers, and then subsequently transform into the final discharge product, Na₂S, preventing the active material from dissolving in the carbonate electrolyte. Consequently, the novel cathode offers a high reversible capacity of 624 mAh g⁻¹ at 0.1 A g⁻¹ and a steady capacity of 395 mAh g⁻¹ at 1 A g⁻¹ for 850 cycles. By constructing the high-kinetics S cathode via the industrialized spray-drying technique, this work will open up a new avenue for superior RT-Na/S batteries in terms of mass production and practical application.

Supporting Information

Supporting Information is available from the Wiley Online Library or from the author.

Acknowledgements

The authors are grateful for financial support from an Australian Renewable Energy Agency (ARENA) Project (G00849), the Innovative Group of Guangdong Province (Grant No. 2014ZT05N013), the National Natural Science Foundation of China (Grant Nos. 11704114, 61427901), and the Australian Research Council (ARC) (DE170100928). Part of the experiments was carried out at the Powder Diffraction Beamline of the Australian Synchrotron. The authors would like to thank Guoqiang Zhao for support on TEM, Dr. Gilberto Casillas-Garcia for support on the STEM technique, and Dr. Tania Silver for critical reading of the paper.

Received: ((will be filled in by the editorial staff))
Revised: ((will be filled in by the editorial staff))
Published online: ((will be filled in by the editorial staff))

References

- [1] a) R. Fang, S. Zhao, Z. Sun, D. W. Wang, H. M. Cheng, F. Li, *Adv. Mater.* **2017**, 29, 1606823; b) S. Xin, Y. X. Yin, Y. G. Guo, L. J. Wan, *Adv. Mater.* **2014**, 26, 1261.
- [2] Y.-X. Wang, B. Zhang, W. Lai, Y. Xu, S.-L. Chou, H.-K. Liu, S.-X. Dou, *Adv. Energy Mater.* **2017**, 7, 1602829.
- [3] S. Wei, S. Xu, A. Agrawal, S. Choudhury, Y. Lu, Z. Tu, L. Ma, L. A. Archer, *Nat. Commun.* **2016**, 7, 11722.
- [4] X. Yu, A. Manthiram, *J. Phys. Chem. C* **2014**, 118, 22952.
- [5] Y. X. Wang, J. Yang, W. Lai, S. L. Chou, Q. F. Gu, H. K. Liu, D. Zhao, S. X. Dou, *J. Am. Chem. Soc.* **2016**, 138, 16576.
- [6] X. Yu, A. Manthiram, *J. Phys. Chem. Lett.* **2014**, 5, 1943.
- [7] Z. Qiang, Y.-M. Chen, Y. Xia, W. Liang, Y. Zhu, B. D. Vogt, *Nano Energy* **2017**, 32, 59.
- [8] D. Ma, Y. Li, J. Yang, H. Mi, S. Luo, L. Deng, C. Yan, M. Rauf, P. Zhang, X. Sun, X. Ren, J. Li, H. Zhang, *Adv. Funct. Mater.* **2018**, 28, 1705537.
- [9] a) S. Zheng, P. Han, Z. Han, P. Li, H. Zhang, J. Yang, *Adv. Energy Mater.* **2014**, 4, 1400226; b) B. W. Zhang, T. Sheng, Y. D. Liu, Y. X. Wang, L. Zhang, W. H. Lai, L. Wang, J. Yang, Q. F. Gu, S. L. Chou, H. K. Liu, S. X. Dou, *Nat. Commun.* **2018**, 9, 4082.
- [10] S. Wei, L. Ma, K. E. Hendrickson, Z. Tu, L. A. Archer, *J. Am. Chem. Soc.* **2015**, 137, 12143.
- [11] a) Z. Li, J. Zhang, Y. Lu, X. W. D. Lou, *Sci. Adv.* **2018**, 4, eaat1687; b) Y. Yao, L. Zeng, S. Hu, Y. Jiang, B. Yuan, Y. Yu, *Small* **2017**, 13.
- [12] P. G. Bruce, B. Scrosati, J. M. Tarascon, *Angew. Chem. Int. Ed.* **2008**, 47, 2930.
- [13] a) S. Zhou, T. Mei, J. Li, W. Pi, J. Wang, J. Li, X. Wang, *J. Mater. Sci.* **2018**, 53, 9710; b) H.-G. Jung, S.-T. Myung, C. S. Yoon, S.-B. Son, K. H. Oh, K. Amine, B. Scrosati, Y.-K. Sun, *Energy Environ. Sci.* **2011**, 4, 1345; c) S.-M. Oh, S.-T. Myung, Y. S. Choi, K. H. Oh, Y.-K. Sun, *J. Mater. Chem.* **2011**, 21, 19368; d) Z. Lin, Q. Xia, W. Wang, W. Li, S. Chou, *InfoMat.* **2019**, 1, 376; e) T. Yang, W. Gao, B. Guo, R. Zhan, Q. Xu, H. He, S.-J. Bao, X. Li, Y. Chen, M. Xu, *J. Mater. Chem. A* **2019**, 7, 150; f) T. Yang, B. Guo, W. Du, M. K. Aslam, M. Tao, W. Zhong, Y. Chen, S.-J. Bao, X. Zhang, M. Xu, *Adv. Sci.* **2019**, 1901557.
- [14] a) X. Yu, A. Manthiram, *ChemElectroChem* **2014**, 1, 1275; b) Y. Hao, X. Li, X. Sun, C. Wang, *ChemistrySelect* **2017**, 2, 9425; c) J. Wang, J. Yang, Y. Nuli, R. Holze, *Electrochem. Commun.* **2007**, 9, 31; d) S. Wenzel, H. Metelmann, C. Reiß, A. K. Dürr, J. Janek, P. Adelhelm, *J. Power Sources* **2013**, 243, 758; e) T. H. Hwang, D. S. Jung, J. S. Kim, B. G. Kim, J. W. Choi, *Nano Lett.* **2013**, 13, 4532; f) Q. Lu, X. Wang, J. Cao, C. Chen, K. Chen, Z. Zhao, Z. Niu, J. Chen, *Energy Storage Materials* **2017**, 8, 77.
- [15] S. Guo, Y. Guo, J. Ren, Y. Zhai, S. Dong, E. Wang, *ACS Nano* **2010**, 4, 4001.
- [16] S. Liu, J. Li, X. Yan, Q. Su, Y. Lu, J. Qiu, Z. Wang, X. Lin, J. Huang, R. Liu, B. Zheng, L. Chen, R. Fu, D. Wu, *Adv. Mater.* **2018**, 30, e1706895.
- [17] X. Yang, F. Xiao, S. Wang, J. Liu, M. K. H. Leung, D. Y. W. Yu, A. L. Rogach, *J. Mater. Chem. A* **2019**, 7, 11877.
- [18] W. Wang, B. Tang, B. Ju, Z. Gao, J. Xiu, S. Zhang, *J. Mater. Chem. A* **2017**, 5, 958.

- [19] Z. Zhu, Y. Xu, B. Qi, G. Zeng, P. Wu, G. Liu, W. Wang, F. Cui, Y. Sun, *Environmental Science: Nano* **2017**, 4, 302.
- [20] A. Douglas, R. Carter, L. Oakes, K. Share, A. P. Cohn, C. L. Pint, *ACS Nano* **2015**, 9, 11156.
- [21] M. Wang, C. Xing, K. Cao, L. Zhang, J. Liu, L. Meng, *J. Mater. Chem. A* **2014**, 2, 9496.
- [22] a) J. Song, M. L. Gordin, T. Xu, S. Chen, Z. Yu, H. Sohn, J. Lu, Y. Ren, Y. Duan, D. Wang, *Angew. Chem. Int. Ed.* **2015**, 54, 4325; b) X. Lu, B. Kirby, W. Xu, G. Li, J. Y. Kim, J. P. Lemmon, V. L. Sprenkle, Z. G. Yang, *Energy Environ. Sci.* **2013**, 6, 299; c) W. Bao, C. E. Shuck, W. Zhang, X. Guo, Y. Gogotsi, G. Wang, *ACS Nano* **2019**, 13, 11500.
- [23] a) E. Thompson, A. E. Danks, L. Bourgeois, Z. Schnepf, *Green Chemistry* **2015**, 17, 551; b) H. Kim, J. T. Lee, A. Magasinski, K. Zhao, Y. Liu, G. Yushin, *Adv. Energy Mater.* **2015**, 5, 1501306; c) W. Zhou, C. Wang, Q. Zhang, H. D. Abruna, Y. He, J. Wang, S. X. Mao, X. Xiao, *Adv. Energy Mater.* **2015**, 5, 1401752.
- [24] a) X. Li, J. Zai, S. Xiang, Y. Liu, X. He, Z. Xu, K. Wang, Z. Ma, X. Qian, *Adv. Energy Mater.* **2016**, 6, 1601056; b) Z. Wang, T. Chen, W. Chen, K. Chang, L. Ma, G. Huang, D. Chen, J. Y. Lee, *J. Mater. Chem. A* **2013**, 1, 2202.
- [25] J. Conder, R. Bouchet, S. Trabesinger, C. Marino, L. Gubler, C. Villevieille, *Nat. Energy* **2017**, 2.
- [26] G. Zhou, H. Tian, Y. Jin, X. Tao, B. Liu, R. Zhang, Z. W. Seh, D. Zhou, Y. Liu, J. Sun, J. Zhao, C. Zu, D. Wu, Q. Zhang, Y. Cui, *PNAS* **2017**, 5, 840.
- [27] W. Xue, Z. Shi, L. Suo, C. Wang, Z. Wang, H. Wang, K. P. So, A. Maurano, D. Yu, Y. Chen, L. Qie, Z. Zhu, G. Xu, J. Kong, J. Li, *Nat. Energy* **2019**, 4, 374.

Figure 1. Schematic illustration of the synthetic process for the $\text{FeS}_2\text{@NCMS/S}$ composite.

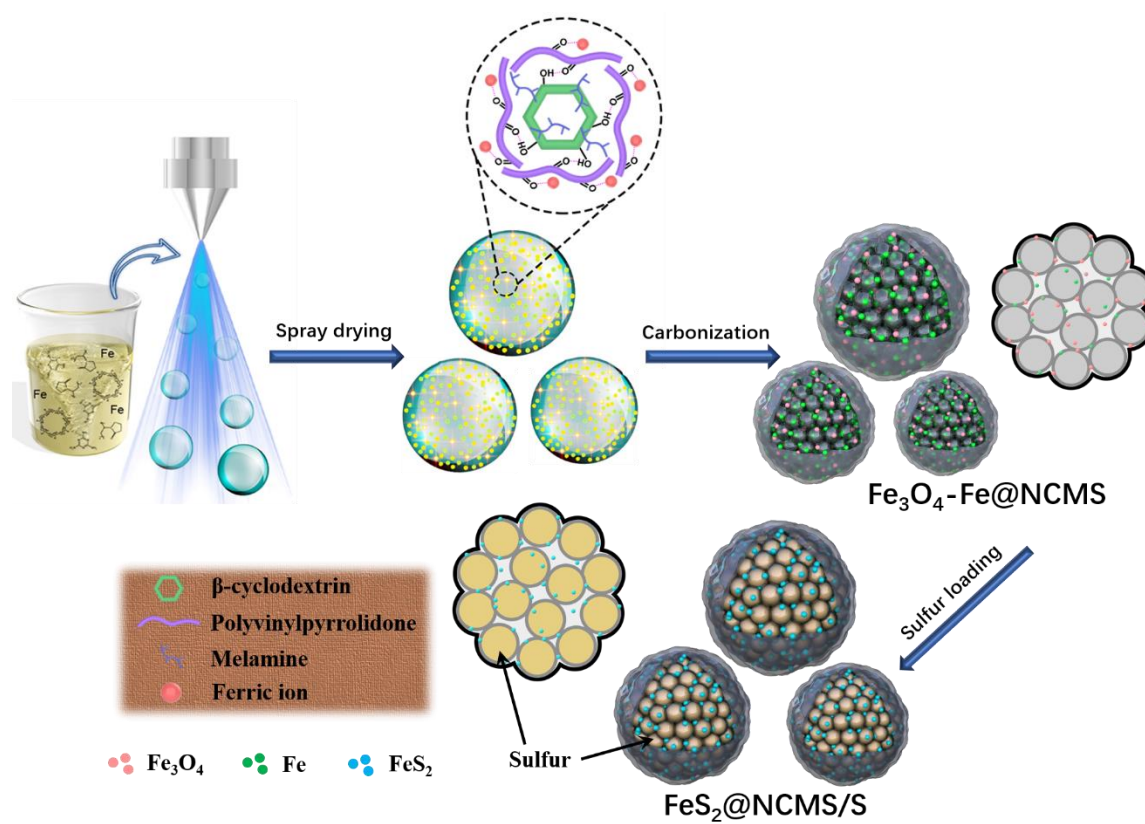


Figure 2. FESEM images at (a) low and (b) high resolution of FeS₂@NCMS/S composite with histogram showing size distribution as inset. (c and d) TEM images of FeS₂@NCMS/S composite. (e) STEM image and (f) HRTEM image of FeS₂@NCMS/S composite. (g) HAADF-STEM image matched with the corresponding molecular model of FeS₂, and (h) corresponding FFT image of FeS₂@NCMS/S composite. (i) STEM-EDS mapping images coupled with EDS line scanning of FeS₂@NCMS/S composite.

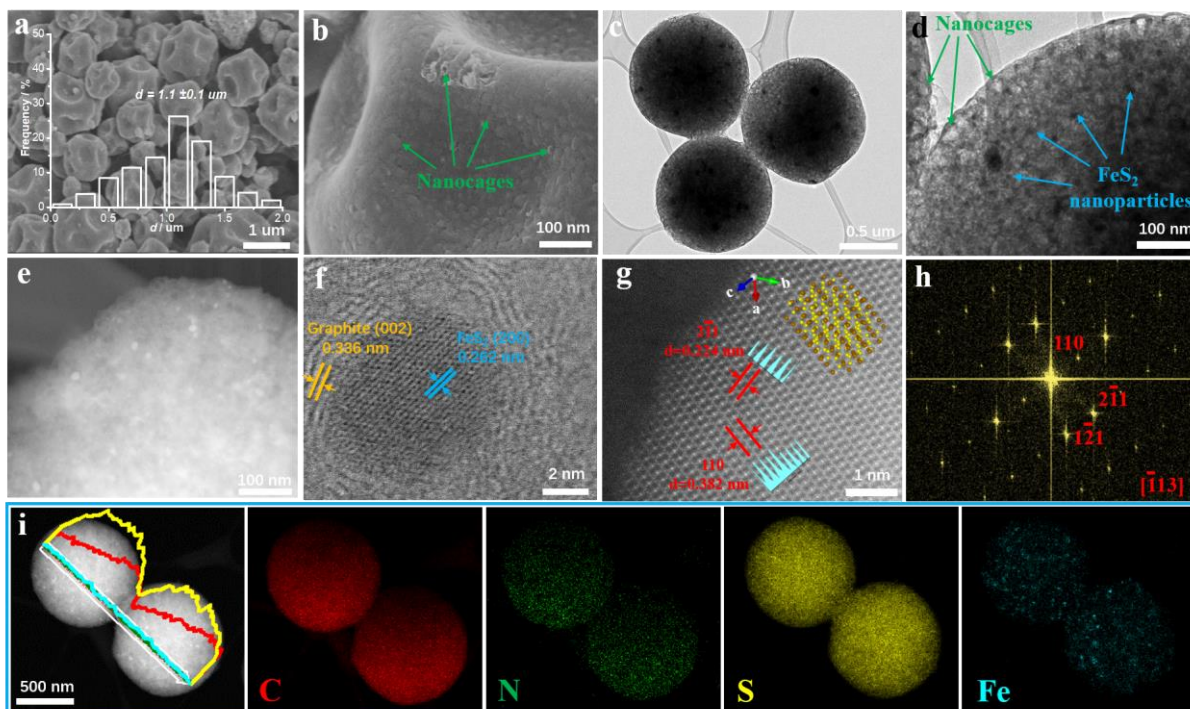


Figure 3. (a) Cyclic voltammograms of FeS₂@NCMS/S composite at 0.1 mV s⁻¹. (b) charge/discharge curves of FeS₂@NCMS/S composite at 0.1 A g⁻¹. (c and d) Cycling performance and rate performance of FeS₂@NCMS/S and NCMS/S, where solid and hollow spheres represent discharge and charge, respectively. (e) Comparison of this work with previously reported RT-Na/S batteries with respect to the rate capability and capacity retention relative to the 2nd cycle after the first 50 cycles (inset).

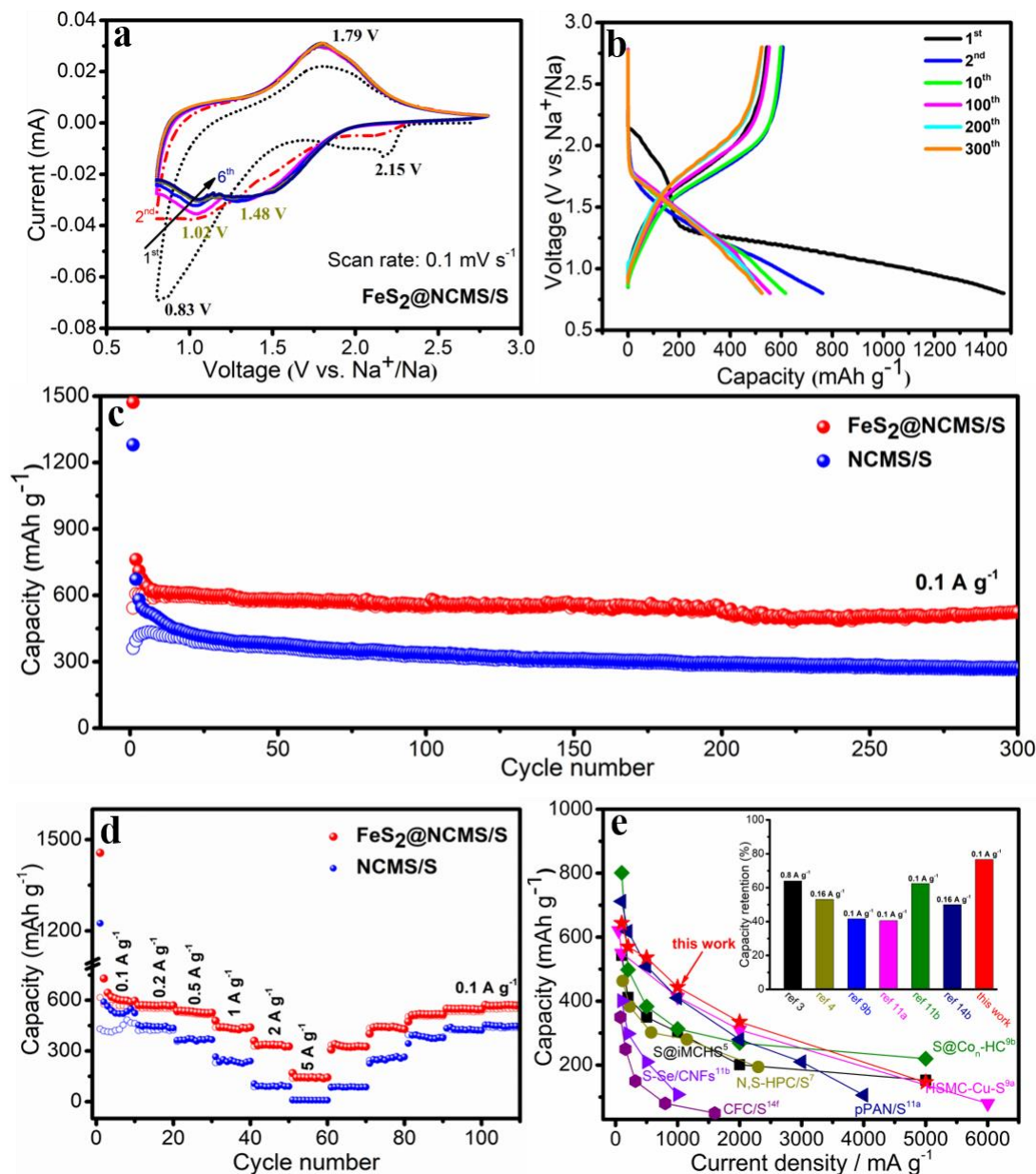


Figure 4. (a) In-situ synchrotron XRD patterns of an RT-Na/S battery containing a $\text{FeS}_2\text{@NCMS/S}$ electrode with the corresponding galvanostatic charge/discharge curves at the current density of 200 mA g^{-1} . (b) Atomic conformations and binding energies for Na_2S_x species adsorption on the FeS_2 (0 0 1) surface. (c) Comparison of the binding energies of various Na_2S_x molecules bound to FeS_2 , N-doped carbon, and pure carbon, respectively, with atomic conformations of Na_2S_4 adsorption on N-doped carbon and pure carbon as insets. (d) Top view schematic representation of corresponding diffusion pathways for FeS_2 . (e) Energy profiles for three different diffusion processes of Na ions on the FeS_2 (0 0 1) surface. Schematic illustration of the sulfur conversion process and the electrocatalytic mechanism of (f) $\text{FeS}_2\text{@NCMS/S}$ and (g) NCMS/S.

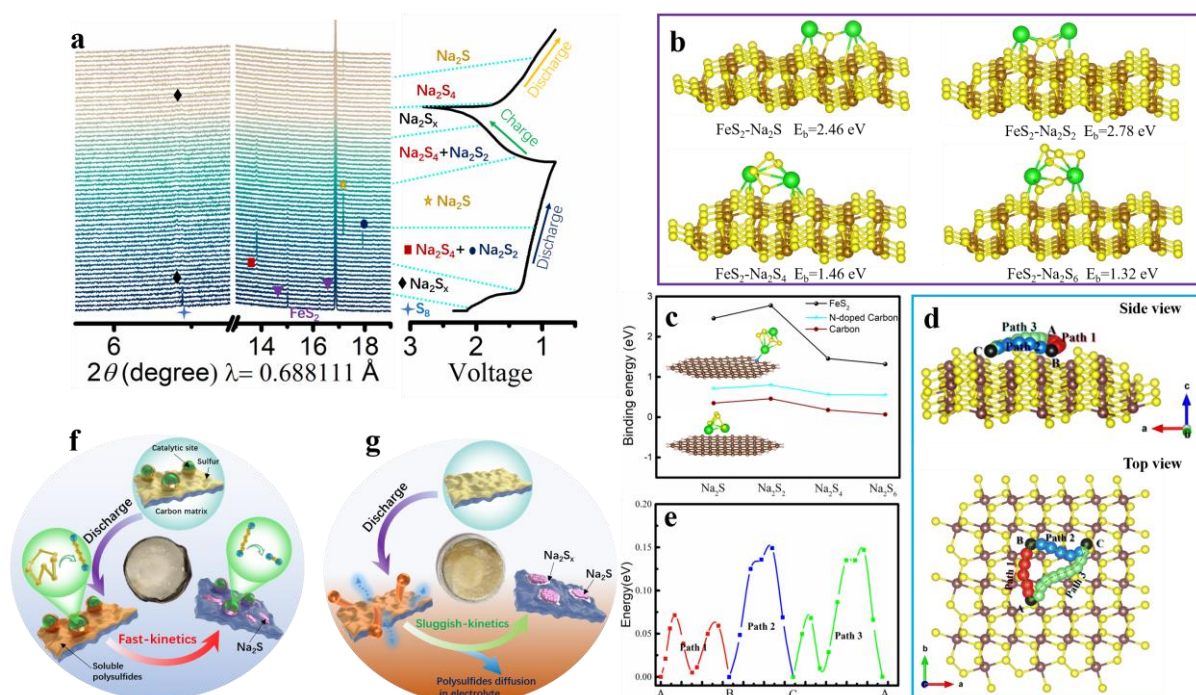
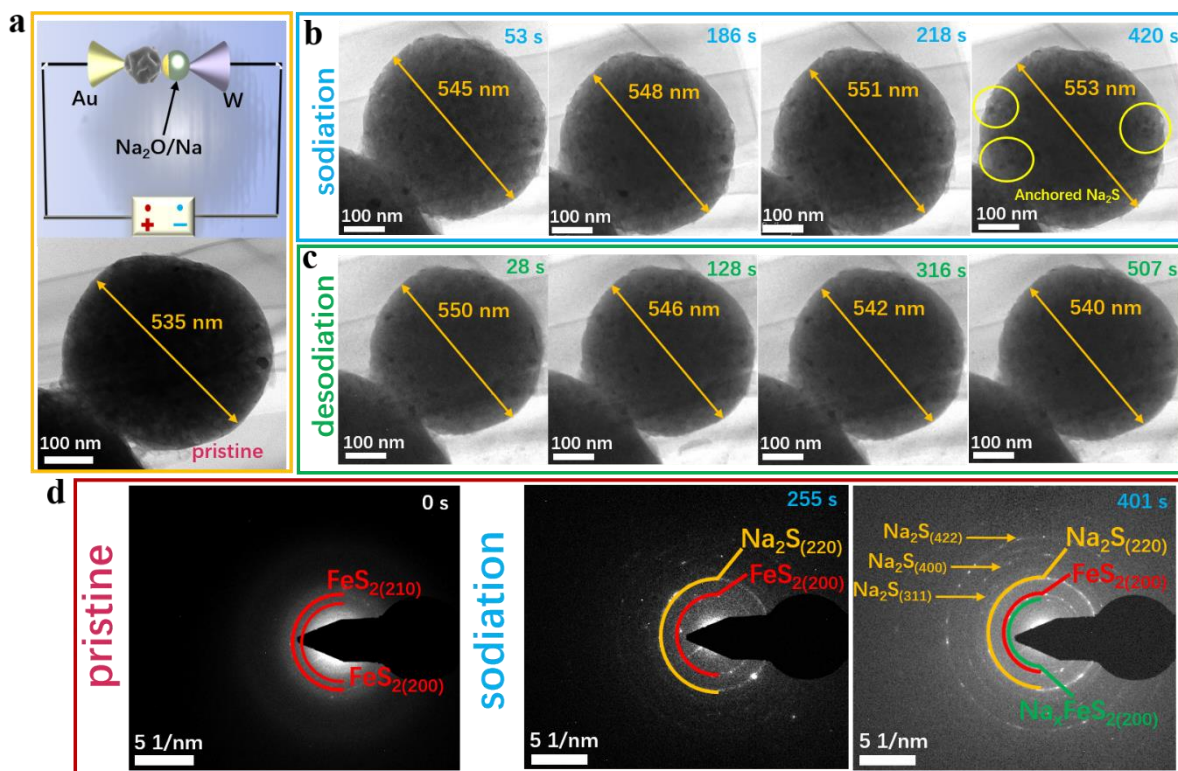


Figure 5. (a) Schematic illustration of in-situ TEM apparatus and pristine image of an individual $\text{FeS}_2\text{@NCMS/S}$ particle. (b and c) Sequential images of $\text{FeS}_2\text{@NCMS/S}$ electrode from in-situ TEM measurements during sodiation and desodiation processes, respectively. (d) In-situ SAED patterns for the $\text{FeS}_2\text{@NCMS/S}$ electrode operated at various states during the initial discharge.



A novel sulfiphilic host, consisting of FeS₂ nanograins grown in-situ in nitrogen-doped hierarchical carbon microspheres, is utilized to realize highly efficient S cathode. The combination of micro-/nano-architectures and FeS₂ nanograins as high affinity sulfur host with multiple physical entrapment to immobilize the polysulfides and achieve reversible conversion of polysulfides towards Na₂S, holding great promise for both scientific research and real application.

Keywords: large-scale production, hierarchical structure, sodium-sulfur batteries, ferrous disulfide, nanograins

Zichao Yan,¹ Yaru Liang,^{2,5} Jin Xiao,³ Weihong Lai,¹ Wanlin Wang,¹ Qingbing Xia,¹ Yunxiao Wang,^{*,1} Qinfen Gu,⁴ Huanming Lu,^{*,5} Shu-Lei Chou,^{*,1} Yong Liu,^{*,6} Huakun Liu,¹ and Shi-Xue Dou¹

High-kinetics sulfur cathode with highly efficient mechanism for superior room-temperature Na-S batteries

